Chemical Engineering Science 302 (2025) 120824

Contents lists available at ScienceDirect

Chemical Engineering Science

journal homepage: www.elsevier.com/locate/ces

CFD simulations of the transition between non-aerated and aerated conditions in uncovered unbaffled stirred tanks

Luca Schembri, Giuseppe Caputo, Michele Ciofalo, Franco Grisafi, Serena Lima, Francesca Scargiali *

Università degli Studi di Palermo, Dipartimento di Ingegneria, Edificio 6, Viale delle Scienze, 90128 Palermo, Italy

ARTICLE INFO

Keywords:
Unbaffled stirred bioreactors
Free surface vortex
Computational fluid dynamics
Multiphase systems
Power number
Volume of fluid

ABSTRACT

The transition between non-aerated and aerated regimes in uncovered unbaffled stirred tanks (UUSTs) was investigated using computational fluid dynamics (CFD). The Volume of Fluid (VOF) method was employed to model the free surface dynamics under various operational conditions. The simulations were able to predict the peculiar experimentally observed behavior of UUSTs and revealed that at velocities below a critical threshold ($N < N_{crit}$), the system remains non-aerated, while exceeding this threshold ($N \geq N_{crit}$) induces bubble ingestion, leading to significant changes in power consumption and flow patterns. The CFD simulations accurately predicted the behaviour of the Power Number (Np) as well as the vortex shape inside the tank both in subcritical and supercritical regimes and showed good agreement with original experimental data and correlations from the literature. Additionally, the modeling of the aerated regime successfully predicted the vortex shape, the bubble dispersion within the tank, and the cavities formed behind the blades.

1. Introduction

Uncovered Unbaffled Stirred Tanks (UUSTs) are gaining significant attention for their interesting performance across diverse industrial sectors such as biochemical, food, oil, chemicals, pharmaceuticals, paper, and power industries. This includes applications in biotechnology, powder dissolution, nuclear fuel processing, wastewater treatment, and so on (Lima et al., 2020; Ramírez-Cruz et al., 2020). These mixers were rarely utilized in industry due to the inherent shortcomings they exhibit: UUSTs, in fact, are limited in mixing effectiveness due to the swirling motions within the fluid, where tangential velocity dominates the flow, resulting in reduced gradients and inadequate axial flow, compared to standard baffled tanks. This swirling motion generates a hollow in the liquid surface within UUSTs, influenced by factors such as impeller design and fluid properties. Notwithstanding these challenges, UUSTs hold promise for specific applications. UUSTs are employed in food and pharmaceutical industries, where vessel cleanness has a primary importance. Another significant advantage of UUSTs is their low power consumption compared to baffled tanks under the same operating conditions. In addition, the gentle stirring in an unbaffled mixing system offers a low shear environment, which promotes the growth of biomass that is normally shear-sensitive (Aloi and Cherry, 1996; Lamberto et al., 1996; Scargiali et al., 2017). Unbaffled vessels are preferred over baffled systems for highly viscous fluids, where baffled systems may lead to the formation of undesired dead zones. Finally, their ability to provide easy aeration and a gentler impact on solids in crystallizers makes them a valuable choice in many scenarios.

Busciglio et al. (Busciglio et al., 2014) investigated mixing rates in unbaffled vessels under free surface vortex using the planar laser induced fluorescence (PLIF) technique. Their results revealed two distinct, partially segregated zones leading to dual mixing dynamics. Unbaffled vessels showed poorer mixing efficiency, with mixing times 2–3 times longer than baffled tanks for the same power input. However, mixing times (10–100 s) were suitable for slower processes. When the vortex bottom approached the impeller plane, mixing efficiencies matched those of baffled tanks, highlighting the broader potential of unbaffled vessels.

As highlighted by Ciofalo et al.(Ciofalo et al., 1996), the depth and shape of the free surface in UUST primarily depend on the impeller's rotational speed. At the same time, additional parameters, for example impeller type and diameter, off-bottom clearance, and physical properties such as viscosity and surface tension, also play significant roles. Busciglio et al. (Busciglio et al., 2013) have classified the flow into various operating conditions based on the position of the lower end of the vortex in relation to the impeller.

* Corresponding author.
E-mail address: francesca.scargiali@unipa.it (F. Scargiali).

https://doi.org/10.1016/j.ces.2024.120824
Received 10 August 2024; Received in revised form 5 October 2024; Accepted 10 October 2024
Available online 11 October 2024

Nomenclature

a	Blade height, [m]
b	Blade width, [m]
c	Off-bottom clearance, [m]
C_1, C_2	Model constants in Eqs. (13) and (14)
C_1', C_2', C_l, $C\mu$	Model constants in Eq. (16)
C_{ij}, C_{kk}	Convection term, [kg m^{-1} s^{-3}]
d	Disk diameter, [m]
d_s	Shaft diameter, [m]
D	Impeller diameter, [m]
D_{Tij}	Turbulent diffusion, [kg m^{-1} s^{-3}]
D_{Lij}	Molecular diffusion, [kg m^{-1} s^{-3}]
F	Body force, [N/m^{-3}]
F_{ij}	Production by system rotation, [kg m^{-1} s^{-3}]
Fr	Froude number
H_1	Liquid level, [m]
H_T	Tank height, [m]
k	Turbulent kinetic energy, [m2/s^{-2}]
N	Impeller speed, [r min^{-1}]
N_p	Power number
p	Static pressure, [Pa]
P	Power consumption, [W]
P_{ij}	Stress production, [kg m^{-1} s^{-3}]
Re	Reynolds number
t	Time [s]
T	Tank diameter, [m]
T_i	Torque, [N m]
u	Fluid velocity vector, [m/s]
u'	Fluid fluctuating velocity, [m/s]

Greek letters

α	Phase volume fraction
β	Coefficient of thermal expansion
δij	Kronecker delta
ε	Turbulence dissipation rate, [m2/s^{-3}]
ε_{ij}	Dissipation tensor in Eq. (7), [kg m^{-1} s^{-3}]
θ	Blade angle to the horizontal plane
κ	Von Kármán constant (= 0.4187)
μ	Viscosity, [kg m^{-1} s^{-1}]
μ_t	Turbulent viscosity, [kg m^{-1} s^{-1}]
ρ	Density, [kg m^{-3}]
τij	Reynolds stress, [kg m^{-1} s^{-2}]
σk	Model coefficient in Eq. (11)
ϕij	Pressure strain, [kg m^{-1} s^{-3}]
$\phi ij,1$	Slow pressure strain, [kg m^{-1} s^{-3}]
$\phi ij,2$	Rapid pressure strain, [kg m^{-1} s^{-3}]
$\phi ij,w$	Pressure strain of wall-reflection term, [kg m^{-1} s^{-3}]

Subscripts

g	Gas phase
i, j, k	Coordinate system
l	Liquid phase
t	Turbulent

Two distinct operational regimes have been identified: sub-critical and super-critical. The sub-critical regime occurs when the rotational speed of the impeller is below a critical threshold ($N < N_{crit}$), meaning that the free surface vortex has not yet reached the impeller blades. In such circumstances, the formation and subsequent bursting of bubbles inside the reactor can be effectively prevented, as air in the headspace is not drawn within the impeller stream (Prakash et al., 2019). This characteristic makes unbaffled vessels potentially helpful for foaming gas–liquid systems, given that the process rates and gas consumption requirements align with the relatively constrained gas transfer rates reachable under these conditions (Scargiali et al., 2014; Tamburini et al., 2021). In contrast, the super-critical regime is characterized by rotational speeds exceeding the critical threshold ($N > N_{crit}$), where the free surface vortex reaches the impeller, allowing the gas phase to be ingested and dispersed inside the reactor. This regime is particularly beneficial in three-phase mixing operations where blockage of gas spargers by solid particles is a frequent problem (Tamburini et al., 2016). Solid particles may cause wear of sparger holes or form a muddy solid residue that blocks the holes, adversely affecting the sparger's performance (Lima et al., 2022). Operating an unbaffled reactor under aerated conditions at velocities above N_{crit}, using a self-ingesting device, can prevent such blockages.

However, it is important to note that under specific circumstances, surface instability phenomena may occur in the use of these mixers, leading to oscillations on the free surface, and potentially adversely affecting agitation and vessel support mechanisms (Busciglio et al., 2016). An increase in impeller speed can cause the system to transition from a sub-critical into a super-critical regime, resulting in significant gas bubble ingestion into the tank. Such a phenomenon also proves to be disadvantageous in certain processes like polymerization, where bubble adhesion to droplets can lead to the formation of poor-quality polymer beads (Tanaka et al., 1986). However, it is noteworthy that this bubble injection phenomenon can be leveraged as a vortex-ingesting (self-induced) system, offering advantages in enhancing mass transfer for bio-hydrogen production (Ngo et al., 2012) or serving as a surface aerator in wastewater treatment applications (Lima et al., 2024; Moucha et al., 2003). However, there is a paucity of studies examining the hydrodynamics of UUSTs compared to standard baffled systems. Research in this area can be categorized into three main domains. Firstly, research focuses on studying and/or modeling the free surface dynamics and on comparing mean tangential velocity profiles with the classical Rankine vortex, as reported by Nagata et al. (Shinji Nagata, 1975). The second set of studies explores employing UUST hydrodynamics in various processes, such as aeration and crystallization. Lastly, the research explores into understanding and enhancing the mixing process within UUSTs, using computational fluid dynamics as well. Numerical modeling of flow in UUSTs presents complexities, as emphasized by Ciofalo et al. (Ciofalo et al., 1996), primarily attributed to strong turbulence anisotropy, streamline curvature, and flow rotation throughout the tank. Unlike baffled tanks, where turbulence is primarily anisotropic only within the impeller stream and largely isotropic in the overall fluid flow, UUSTs display a more complex flow regime. Moreover, conventional approaches like the Reynolds-Averaged Navier–Stokes (RANS) method employing common eddy viscosity turbulence models struggle to accurately capture secondary flows and impeller discharge areas in UUSTs.

Numerous numerical studies existing in literature adopt the RANS approach. Haque et al. (Haque et al., 2006), Glover et al. (Glover and Fitzpatrick, 2007) and Mahmud et al. (Mahmud et al., 2009) have attempted to improve accuracy in the numerical studies. Haque et al. and Mahmud et al. employed a second-moment differential Reynolds-stress turbulence Model (RSM) and the Shear Stress Transport (SST) eddy viscosity model, demonstrating a more accurate prediction of bulk fluid motion. Mahmud et al. (Mahmud et al., 2009) demonstrated that these models often underestimate the size of the discharge zone and fail to accurately capture the dynamics of the free surface. While the predicted overall shape of the liquid free surface matches well with measurements, the vortex depth is not accurately predicted. The RSM model shows a good match between the measured and predicted axial and tangential velocities, but it significantly underestimates the radial velocity. Predictions of turbulent kinetic energy align reasonably well with

measurements in the bulk flow region, although there is a noticeable discrepancy near the reactor wall where this quantity is underpredicted.

Additionally, the RSM model provides better predictions of the locations of the velocity peak, i.e., the boundary between the forced- and free-vortex regions. Furthermore, the RSM model predicted axial and radial velocities in better agreement with measurements than the SST model. Recently, the Unsteady Reynolds-Averaged Navier–Stokes (URANS) method has been utilized with these types of problems. The advantage of URANS lies in its capability to capture part of the unsteady behavior periodically induced by the impeller motion, resulting in more accurate outcomes compared to the conventional RANS approach (Zamiri and Chung, 2017).

Large-Eddy Simulation (LES) has emerged as a powerful tool for resolving flow dynamics within stirred tanks, as demonstrated by Derksen and Van den Akker (Derksen and Van Den Akker, 1999). Alcamo et al. (Alcamo et al., 2005) further showed the utility of LES in understanding complex turbulent flow fields within industrial-scale, unbaffled tanks stirred by a Rushton turbine. Their study utilized the Smagorinsky model to capture unresolved subgrid scales, achieving numerical predictions that closely matched experimental data obtained via Particle Image Velocimetry (PIV) and literature results, particularly in terms of mean tangential velocities. LES excels in capturing macro instabilities, flow anisotropy, and trailing vortex structures near the impeller blades, pivotal to the mixing process. These attributes make LES particularly effective for modeling the flow within Uncovered Unbaffled Stirred Tanks. Despite being promising, there remains a lack of studies utilizing LES for UUST analysis. Lamarque et al. (Lamarque et al., 2010) worked with LES application in UUSTs, investigating a flow precipitator mixed with a rod at the tank bottom. Their research produced promising outcomes, as the average and fluctuating velocities closely matched experimental Laser-Doppler velocimetry measurements and coherent turbulent structures revealing insights into mixing dynamics using the Q-criterion, which identifies regions where the fluid follows a closed rotational path. Similarly, Bertrand et al. (2012a) investigated into UUST flow analysis, highlighting anisotropic regions within the tank using Lumley's Triangle (Escudié and Liné, 2006) and elucidating their impact on the precipitation process. Notably, these studies, while informative, deviate from industry-standard impeller configurations.

Moreover, the computational mesh often lacks the resolution necessary to precisely capture both mean and fluctuating velocities in the central region of the tank near the impeller. Deshpande et al. (Deshpande et al., 2017) employed Large-Eddy Simulations (LES) in a vessel stirred by a Rushton turbine using the free open-source computational fluid dynamics (CFD) software package OpenFOAM (Open Source Field Operation and Manipulation), and likened power consumption with the findings of Scargiali et al. (Scargiali et al., 2014). Although LES proves to be effective in resolving flow within UUSTs, its computational demands are challenging. Firstly, the mesh size required for a high-quality solution is significant. Secondly, considerable time is needed to develop the flow and deform the free surface, increasing computational costs. While, in LES or URANS studies of standard baffled tanks, approximately twenty revolutions of the impeller are typically needed to establish flow, UUST simulations may require over 100 impeller revolutions, emphasizing the importance of simulation time (Ramírez-Cruz et al., 2020). Furthermore, accurate modeling of the free surface in UUSTs is essential due to flow pattern alterations induced by surface deformation driven by the impeller-induced flow dynamics. Thus, as highlighted by Ciofalo et al. (Ciofalo et al., 1996), accurately predicting the surface shape in Uncovered Unbaffled Stirred Tanks is complex and serves as a crucial validation metric for overall flow field simulations. Their pioneering work attempted to model UUSTs using a body-fit method to simulate liquid surface deformation, necessitating an iterative process to achieve a steady-state solution under a zero-stress condition in the normal direction. Subsequent research has favored the Volume of Fluid (VOF) method for solving flow dynamics within UUSTs (Jiao et al., 2024). Additionally, a hybrid VOF-Eulerian-Eulerian model was employed by Haque et al. (Haque et al., 2006) and Mahmud et al. (Mahmud et al., 2009). The primary challenge with these methods arises from representing the liquid volume fraction across a broad range from 0 to 1. Consequently, the validation test can be somewhat misleading. In contrast, Bertrand et al. (2012b) employed a Lagrangian approach known as Discontinuous Front-Tracking (DFT), which can achieve high accuracy given a finely detailed mesh. However, this precision may come at the cost of increased computational demands.

The primary objective of this study is to assess the fluid dynamics established in UUSTs under both sub-critical and supercritical conditions and to reproduce the unique experimental behavior, previously observed by the same authors, of power consumption under varying operating conditions, such as changes in the rotational speed of the Rushton impeller and relevant aeration conditions. Additionally, the study aims to correctly predict the vortex shape in these systems under both non-aerated and aerated conditions. To achieve this objective, various computational fluid dynamics (CFD) simulations were conducted using the Volume of Fluid method. These simulations enable adequate assessments of the free surface shape in a biphasic system in the absence and presence of bubble ingestion and the flow patterns generated by this radial impeller design.

2. Materials and methods

The mixing system investigated in this study is showed in Fig. 1.*a*. The system comprises a flat-bottomed cylindrical tank equipped with a standard Rushton turbine for stirring. The working fluid utilized was water, with a density $\rho_l = 998 kgm^{-3}$ and a viscosity $\mu_l = 0.00102 Pa \bullet s$. The initial liquid level was set to $H = T$. Detailed geometrical dimensions of the stirred vessel are provided in Table 1.

To account for the formation of a vortex at the liquid surface during stirring, an air zone with a density $\rho_g = 1.225 kgm^{-3}$ and a viscosity of $\mu_l = 1.79 \times 10^{-5} Pa \bullet s$ was introduced above the liquid level. This air zone had a height of $H_g = 0.11m$ to prevent the liquid from spilling out of the tank.

2.1. Geometrical modeling

The initial phase of the simulation involved geometric modeling and the creation of body-fitted grids using the mesh tools within Ansys Workbench® software (Ansys Inc, USA). The fluid domain was partitioned into two sections, namely, *fluid-domain-zone* and *fluid-subdomain-zone*, containing the impeller. To simulate the impeller rotation, a moving reference frame was applied to the impeller zone and a sliding mesh approach was used to manage the relative motion between the rotating and stationary zones. As shown in Fig. 1.*b,* the common interface of the two zones was placed at $r = 0.04$ m and 0.049_m_<_z_<0.077_m. The region of the subdomain circumscribed to the impeller has been highlighted in red.

2.2. Mathematical model

2.2.1. The governing equations

The following momentum and continuity equations were solved across the entire fluid domain:

$$\frac{\partial \rho}{\partial t} = \nabla \bullet (\rho \, \mathbf{u}) = 0 \tag{1}$$

$$\frac{\partial}{\partial t}(\rho \boldsymbol{u}) + \nabla \bullet (\rho \, \mathbf{u}\mathbf{u}) = -\nabla p + \nabla \bullet \left[\mu\left(\nabla \mathbf{u} + \nabla \mathbf{u}^{\mathrm{T}}\right)\right] + \rho \boldsymbol{g} + \boldsymbol{F} \tag{2}$$

where t is the time, $\mathbf{u}$ is the mixture velocity, p is the static pressure, $\boldsymbol{g}$ is gravitational acceleration and $\boldsymbol{F}$ is body force. ρ and μ are respectively mixture density and dynamic viscosity, described in the following section.

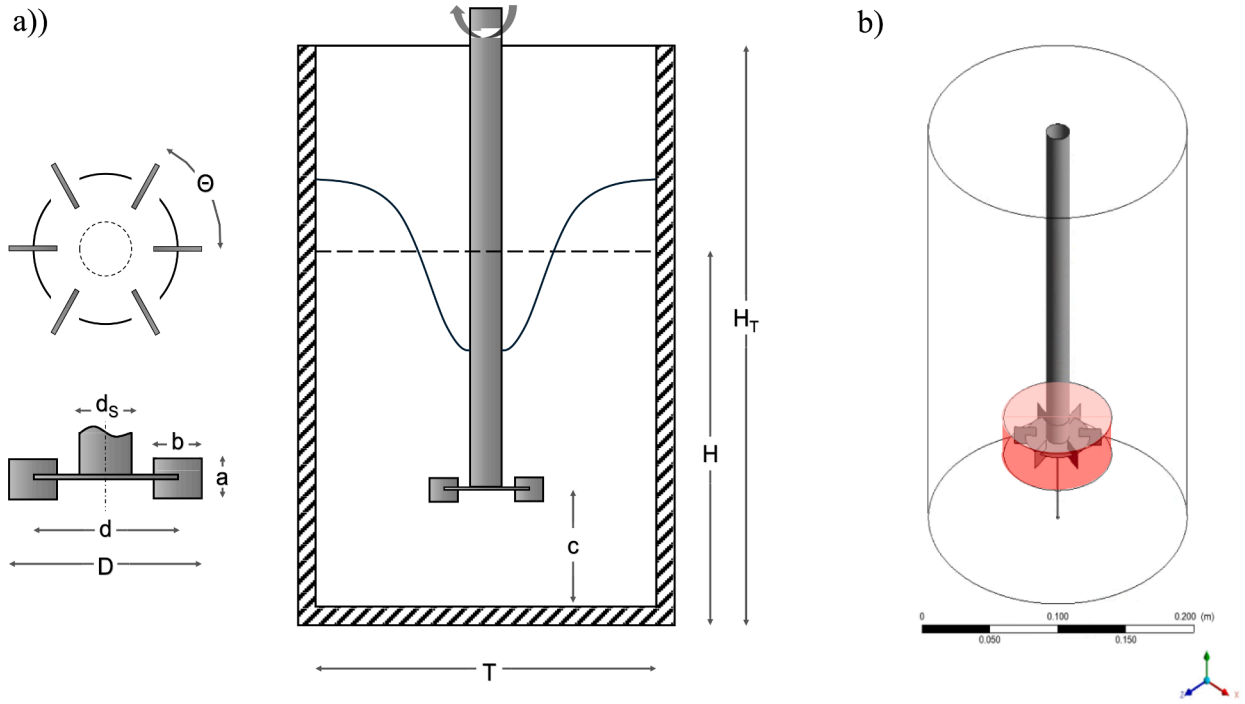

Fig. 1. The adopted mixing system: (a) Stirred tank and Rushton turbine; (b) Geometrical domain with the fluid-subdomain-rotating-zone highlighted in red.

Table 1
Dimensions of the stirred tank utilized.

Geometry	Symbol	Value
Tank diameter	T	0.19 m
Tank height	H_T	0.30 m
Liquid level	H	T
Impeller diameter	D	T/3
Off-bottom clearance	c	T/3
Blade height	a	D/5
Blade width	b	D/4
Disk diameter	d	¾ D
Shaft diameter	d_S	0.017 m
Blade Angle	Θ	60°

2.2.2. The volume of fluid model

Under stirring conditions, near to the free surface, the formation of a central vortex occurred which curved the surface itself in the direction of the impeller(Li et al., 2017; Płusa et al., 2021). By solving a set of continuity equations, the VOF method can model two or more immiscible *Eulerian Phases* to find out the volume fraction (α) in each computational cell (Li and Xu, 2017). The properties and variables of any given cell are affected by its volume fraction values. Each cell is characterized by either air $(\alpha_g = 1)$, water $(\alpha_g = 0)$ or a blend of water and air $(0 < \alpha_g < 1)$. Properties and variables were allocated to each cell within the solution domain according to the local volume fraction of each phase. The conservation of volume fraction for the generic phase i (α_i) can be determined for incompressible phases and no inter-phase mass transfer by:

$$\frac{\partial \alpha_i}{\partial t} + \boldsymbol{u} \bullet \nabla(\alpha_i) = 0 \tag{3}$$

In each control cell, the mixture's volume fraction and physical properties were constrained as follows:

$$\alpha_g + \alpha_l = 1 \tag{4}$$

$$\rho = \rho_l \alpha_l + \rho_g \alpha_g \tag{5}$$

$$\mu = \mu_l \alpha_l + \mu_g \alpha_g \tag{6}$$

2.2.3. The turbulence model

Turbulent flows are characterized by fluctuating velocity fields, which in turn lead to fluctuations in the transported variables. These fluctuations encompass a wide range of scales and frequencies, making direct modeling difficult. As an alternative, to describe the turbulent flow one can use Reynolds-averaged Navier-Stokes (RANS) models, including eddy viscosity models (such as k–ε or k–ω), and Reynolds Stress transport models (RSM) (Montante et al., 2006).

Before evaluating grid independence, a systematic study was conducted to select the most appropriate turbulence model. This was achieved by comparing the free surface profile evaluated through the Nagata correlation (Shinji Nagata, 1975), as refined by Ciofalo et al. (Ciofalo et al., 1996), with solutions obtained from a series of preliminary simulations using various turbulence models with an intermediate grid: the standard k–ε model (Launder and Spalding, 1974), the k–ω SST (Shear Stress Transport) model (Menter et al., 2003), and two versions of a Reynolds Stress transport model (RSM), using either a linear pressure-strain correlation approximation (RSM-LPSM) or a quadratic pressure-strain correlation approximation (RSM-QPSM). The former version is essentially that proposed in 1975 by Launder et al. (1975), the latter is the variant introduced in 1991 by Speziale et al (Speziale et al., 1991). All the above models are implemented as standard options in Ansys-Fluent®(ANSYS Inc., 2021).

Comparative results concerning the vortex shape are shown in Fig. 2 for 400 RPM, liquid viscosity equal to 0.001_Pa·s. The eddy-viscosity RANS models (k-ε and SST) exhibit inefficiencies in predicting the vortex shape accurately. The seven-equation Reynolds Stress Models, especially RSM-LPSM, yield a better agreement with the empirically-based profile reported by Nagata. The RSM-QPSM predicts an irregular diffused liquid–air interface which is not exhibited by the experiments at this rotational speed and liquid viscosity (Michalcová and

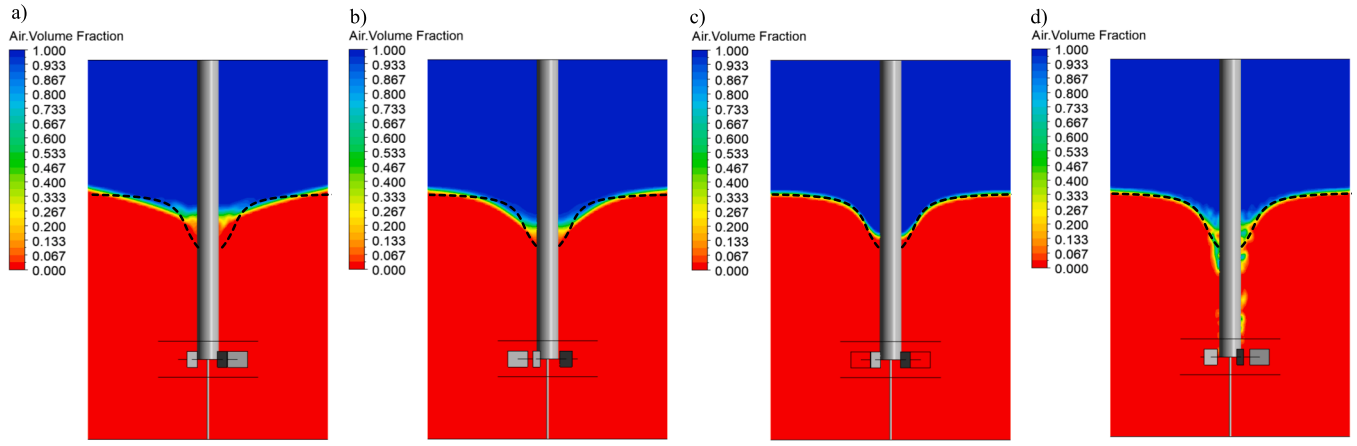

Fig. 2. Air volume fraction maps at 400 RPM (liquid viscosity of 0.001 Pa·s) for different turbulence models considered: a) k-ε; b) k-ω SST; c) RSM LPSM; d) RSM QPSM. Black dashed line: Nagata correlation.

Kotrasová, 2020).

In addition to vortex shape analysis, the evaluation included consideration of the *Np* value, which can be assessed either from the torque exerted by the impeller or from the computed dissipation (ε), which represents the rate at which the fluid's turbulent kinetic energy is converted into thermal energy due to viscous forces. This comparison is shown in Fig. 3. It is clear that the values of *Np* computed by the two independent methods practically coincide only when the RSM models are used, while they broadly diverge when eddy-viscosity models (especially the *k-ε*) are adopted. In addition, only the RSM models yield *Np* values in agreement with the experimental data and relevant empirical correlation proposed by Scargiali et al. (Scargiali et al., 2013) ($Np = 19.5Re^{-0.3}$).

As a result of the study, the RSM LPSM emerged as the optimal turbulence model. Therefore, it was selected for the grid independence assessment.

The Reynolds stress transport equations in the RSM-LPSM model are (Launder et al., 1975):

$$\frac{\partial \tau_{ij}}{\partial t} + \frac{\partial u_k \tau_{ij}}{\partial x_k} = D_{T,ij} + D_{L,ij} + P_{ij} + \phi_{ij} + \varepsilon_{ij} + F_{ij} \tag{7}$$

where τ_{ij} is the generic the Reynolds Stress, defined as $\tau_{ij} = \rho\overline{u_i' u_k'}$. $D_{T,ij}$ is the turbulent diffusion, $D_{L,ij}$ is molecular diffusion, P_{ij} is the stress production. The term ϕ_{ij} accounts for the pressure-strain correlation, ε_{ij} represents dissipation and F_{ij} is the production due to system rotation. The terms $D_{L,ij}$, P_{ij} and F_{ij} do not necessitate any modeling, and have the following expressions:

$$D_{L,ij} = \frac{\partial}{\partial x_k}\left[\mu \frac{\partial}{\partial x_k}\left(\overline{u_i' u_j'}\right)\right] \tag{8}$$

$$P_{ij} = -\rho\left(\overline{u_i' u_k'}\frac{\partial u_j}{\partial x_k} + \overline{u_j' u_k'}\frac{\partial u_i}{\partial x_k}\right) \tag{9}$$

$$F_{ij} = -2\rho\Omega_k\left(\overline{u_j' u_m'}\varepsilon_{ikm} + \overline{u_i' u_m'}\varepsilon_{jkm}\right) \tag{10}$$

The impeller region was simulated using a rotating reference frame, where Ω_k is equal to the impeller rotational velocity. The terms $D_{T,ij}$, ϕ_{ij},

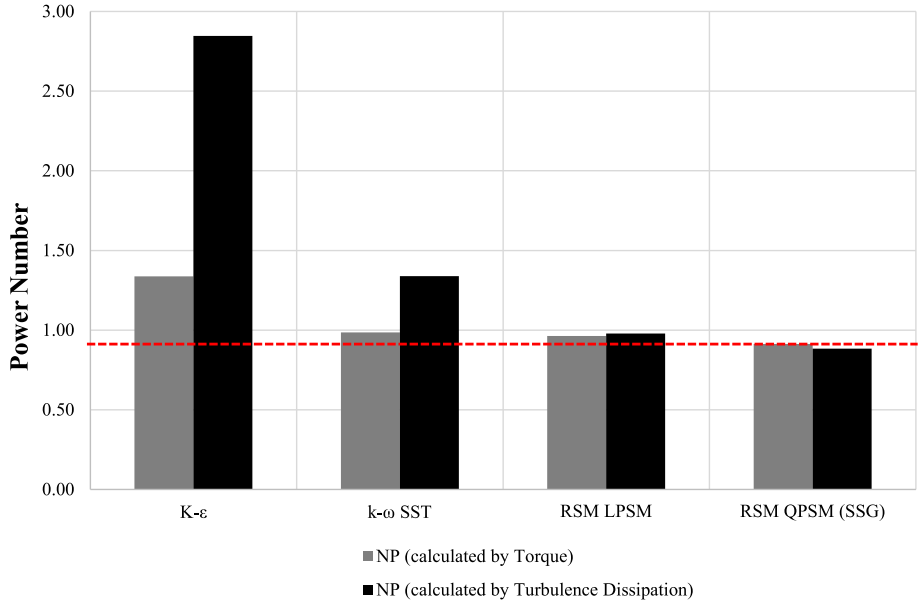

Fig. 3. Power Number (Np) at 400 RPM for different turbulence models: k-ε, k-ω SST, RSM LPSM, and RSM QPSM. Grey bars: Np calculated using torque; black bars: Np calculated using turbulence dissipation. Red dashed line: reference Power Number.

ε_{ij} required modelling to close the set of Eq. (7). For the turbulent diffusion $D_{T,ij}$ the simplified model authored by Daly and Harlow (Daly and Harlow, 1970) was adopted:

$$D_{T,ij} = \frac{\partial}{\partial x_k}\left(\frac{\mu_t}{\sigma_k}\frac{\partial \overline{u_i' u_j'}}{\partial x_k}\right) \tag{11}$$

where σ_k (turbulent Prandtl number for k) was set to 0.82 (Lien and Leschziner, 1994).

The pressure-strain term ϕ_{ij} was divided into three components as proposed by Gibson and Launder (Gibson and Launder, 1978), Fu et al. (Fu et al., 1988), and Launder (Launder, 1989):

$$\phi_{ij} = \phi_{ij,1} + \phi_{ij,2} + \phi_{ij,w} \tag{12}$$

where $\phi_{ij,1}$ is labelled slow pressure-strain term, $\phi_{ij,2}$ rapid pressure-strain term, and $\phi_{ij,w}$ wall-reflection term. The slow and rapid pressure-strain terms are modeled as:

$$\phi_{ij,1} = C_1 \rho \frac{\varepsilon}{k}\left[\overline{u_i' u_j'} - \frac{2}{3}\delta_{ij}k\right] \tag{13}$$

$$\phi_{ij,2} = C_2\left[\left(P_{ij} + F_{ij} - C_{ij}\right) - \frac{1}{3}\delta_{ij}\left(P_{kk} - C_{kk}\right)\right] \tag{14}$$

where $C_1 = 1.80$, $C_2 = 0.60$. P_{ij} and F_{ij} are defined by Eqs. (9) and (10). C_{ij} is the convection term:

$$C_{ij} = \frac{\partial}{\partial x_k}\left(\rho u_k \overline{u_i' u_j'}\right) \tag{15}$$

The term $\phi_{ij,w}$ is responsible for the redistribution of normal stress near the wall and is represented by the following model:

$$\begin{aligned}\phi_{ij,w} = {} & C_1' \frac{\varepsilon}{k}\left(\overline{u_k' u_m'} n_k n_m \delta_{ij} - \frac{3}{2}\overline{u_i' u_k'} n_j n_m - \frac{3}{2}\overline{u_j' u_k'} n_j n_k\right)\frac{C_l \kappa^{\frac{3}{2}}}{\varepsilon d} \\ & + C_2' \frac{\varepsilon}{k}\left(\phi_{km,2} n_k n_m \delta_{ij} - \frac{3}{2}\phi_{ik,2} n_j n_m - \frac{3}{2}\phi_{jk,2} n_j n_k\right)\frac{C_l \kappa^{\frac{3}{2}}}{\varepsilon d}\end{aligned} \tag{16}$$

where $C_1' = 0.50$, $C_2' = 0.30$. n_k is the x_k component of the unit vector normal to the wall, d is the normal distance to the wall, and $C_l = C_\mu^{\frac{3}{4}}/k$, where $C_\mu = 0.09$ and κ is the von Kármán constant, assumed equal to 0.4187. The dissipation tensor ε_{ij} is modeled as isotropic:

$$\varepsilon_{ij} = \frac{2}{3}\delta_{ij}\rho\varepsilon \tag{17}$$

The scalar dissipation rate ε can be determined using a transport equation like that in the standard $k-\varepsilon$model.

2.3. Mesh and grid independence study

The fluid domain was discretized using structured hexahedral grids, chosen for their ability to yield a satisfactory convergence with a moderate number of finite volumes. This type of grid offers higher accuracy and computational efficiency compared to tetrahedral grids, which is particularly beneficial in simulations involving advection-dominated flows where reduced numerical diffusion is critical (Michalcová and Kotrasová, 2020). Hexahedral grids align better with primary flow directions, thereby improving solution accuracy and stability.

To ensure the simulation's accuracy, the grids were refined in critical areas such as blades and tank walls. Grid independence was rigorously tested by approximately halving and doubling the number of volumes compared to the *Fine grid* configuration (Fig. 4) along each of the three cylindrical directions (azimuthal, vertical and radial). This investigation spanned a range from 990,000 to 4,000,000 finite volumes. The analysis concerned the comparison of a global quantity, such as the power number. As shown in Table 2, the relative error between the fine and the very fine grids was found lower than 4 %, supporting the selection of the

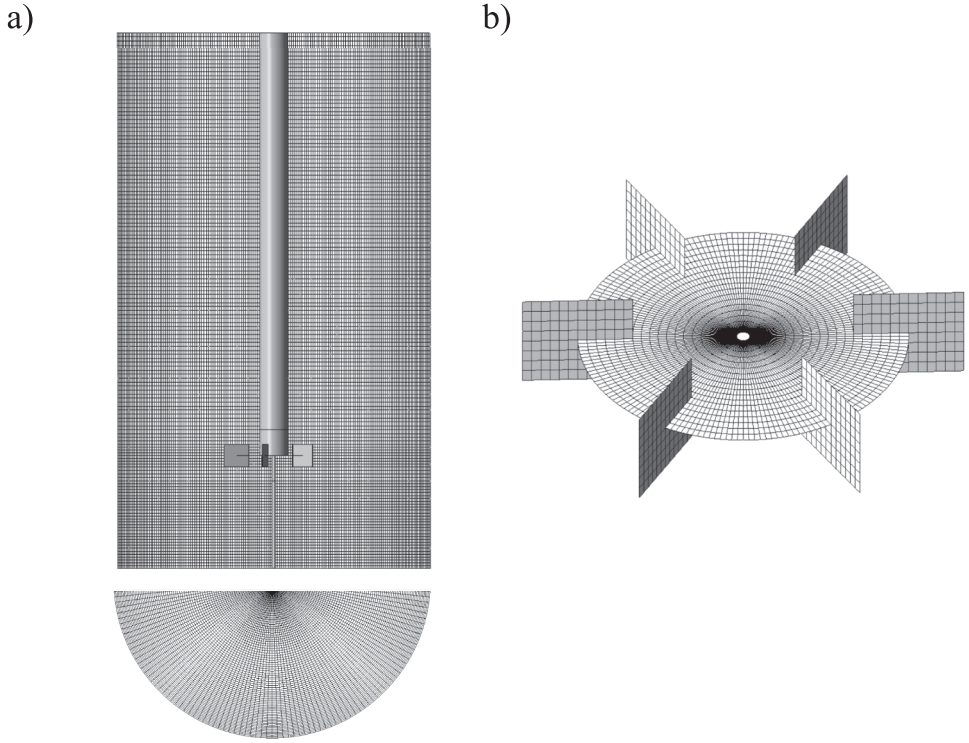

Fig. 4. Computational Domain: (a) Adopted Mesh; (b) Detailed view of the impeller mesh, specifically focusing on the simulated Rushton Turbine.

Table 2
Grid independence study for CFD simulations performed using the RSM LPSM turbulence model, with an impeller speed of 400 RPM and a liquid viscosity of 0.001 Pa s. "Coarse grid" and "very fine grid" indicate approximately the halving and doubling of the number of volumes compared to the Fine grid configuration.

Mesh	Number of volumes	Power Number	Relative error (%)
1 – Coarse grid (azimuthal)	794,304	1.481	59.9 %
2 – Coarse grid (vertical)	992,880	1.343	45.0 %
3 – Coarse grid (radial)	992,880	1.414	52.7 %
4 – Fine grid	1,985,760	0.962	3.9 %
6 – Very fine grid (azimuthal)	3,971,520	0.926	0.0 %
7 – Very fine grid (radial)	3,971,520	0.938	1.3 %
5 – Very fine grid (vertical)	3,971,520	0.955	3.1 %

fine grid as a balanced choice in terms of accuracy and computational efficiency. Furthermore, the power number obtained with the chosen grid showed good agreement with the experimental value of 0.93 (Scargiali et al., 2013), confirming the reliability of the simulation results with this configuration.

2.4. Computational details

Time-dependent computational fluid dynamics simulations were conducted using the commercial software *Ansys Fluent V23R2* by Ansys® Inc (ANSYS Inc., 2021). The initial time step was set to 0.00083 s, corresponding to the time required for a 2-degree rotation, which aligned with a circumferential division of the mesh when the impeller operates at a speed of 400 RPM. Each time step involved 15 iterations. A phase-coupled SIMPLEC algorithm was employed to manage the velocity–pressure coupling. The volume fraction was discretized using a compressive scheme, while pressure was discretized using a PRESTO! scheme. Second-order upwind schemes were employed to discretize the momentum equations, turbulence kinetic energy, and turbulence dissipation rate. Initially, the fluid was at rest and the free liquid surface was located at a height $H = T$.

Regarding the boundary conditions, the velocities at the tank's bottom and sidewalls were fixed at zero, and a standard wall function was utilized to simulate fluid flow near the walls. The impeller zone was resolved using a sliding mesh approach, with a specific rotational velocity imposed on the impeller. In contrast, the stationary zone was resolved using a stationary reference frame. Within the moving reference frame, the impeller blades were treated as stationary walls. The top of the vessel was designated as a pressure-outlet boundary condition with a gauge pressure of zero.

The simulation runtime depends on reaching the steady state for each specific rotational speed adopted (value between 200 and 1200 RPM. The attainment of the steady state was assessed by evaluating the Power Number and its invariance over time. It was observed that the time to reach the steady state condition decreases as the rotational speed increases. Upon achieving final convergence, all the residuals were less than $1{\cdot}10^{-4}$ for all simulations. The simulations took approximately 3 ÷ 5 week to run on the following system specifications: Windows 10 Enterprise 64-bit (10.0, build 19045); Processor: Intel(R) Xeon(R) CPU E5-2640 v3 @ 2.60 GHz (32 CPUs), ~2.6 GHz; Memory: 65536 MB RAM.

3. Results and discussion

3.1. Power consumption

The experimental specific power dissipation values, sourced from Scargiali et al. (Scargiali et al., 2013), were obtained at different agitation velocities using a static frictionless turntable. CFD simulations of the same system were conducted. Four viscosities were selected for this study: 0.001_Pa·s, 0.00285_Pa·s, 0.000707_Pa·s, and 0.00152_Pa·s. The experimental results reported in (Scargiali et al., 2013) are presented in Fig. 5.*a* and the four cases are shown from the lowest viscosity (distilled water, 0.001 Pa·s) to the highest viscosity case (water-polyvinylpyrrolidone solution, 0.0152_Pa·s).

As shown, bold black symbols indicate the critical rotational speeds *(N_{crit})* when the free surface vortex reached the impeller blade. Experimental observations of the reactor revealed that at rotational speeds below N_{crit}, no bubbles were present in the liquid phase. However, once N_{crit} was exceeded, air was drawn into the system from the free surface vortex, causing a dispersion of bubbles within the liquid. As shown in Fig. 5.*a,* a steep decrease in power dissipation with agitation speed occurred across all configurations.

The authors (Scargiali et al., 2013) reported that for rotational velocities below N_{crit}, the specific power dissipation increased with agitation speed, following a power law with an exponent of approximately 3. Above the critical agitation speed, a noticeable decrease in the power law exponent occurred, due to the dispersed gas phase present in the vessel. According to several studies, this behaviour could be attributed to the formation of gas pockets behind the stirrer blades (Maluta et al., 2023; Nienow et al., 1985). Another phenomenon visually observed, which affected the mechanical power demand, was that as velocity increased in uncovered unbaffled tanks, a progressively larger portion of the impeller blades came in contact with the vortex and therefore with the gas phase overlying the liquid. Consequently, these submerged blades were no longer in contact with the liquid phase and thus ceased to contribute to torque generation. The total power dissipation was converted into power number N_p values, defined as:

$$N_p = \frac{P}{\rho_L N^3 D^5} \tag{18}$$

where P is agitation power [W], ρ_L is liquid density [kg m^{-3}], N is agitation speed [s^{-1}] and D is impeller diameter [m]. Power number results were reported in Fig. 5.*b* for the four liquid viscosities investigated. The power number remained nearly constant or slightly decreased until the free surface vortex reached the impeller (non-aerated regime, $N\_ < \_N_{crit}$), consistent with observations by Ruston et al. (Rushton et al., 1950). Subsequently, a distinct decrease in the power number was noted after the vortex reached the impeller and air bubbles started dispersing inside the reactor ($N\_ > \_N_{crit}$). Upon reaching critical conditions, the dependence of N_p on the Reynolds number follow a power law that closely resembled simple inverse proportionality. In this regime, the phenomena already discussed affecting power demand gave rise to a quite dependence of N_p on Re, leading to a simple proportionality between P and N^2.

3.2. CFD simulation results on power number

In order to evaluate the Power Number *(Np)* calculated through Eq. (18), it was necessary to assess the power consumption value as a function of the impeller's rotational speed and the viscosity of the liquid under consideration.

For each simulation step, the dissipated power was calculated as follows:

$$P = N \bullet \sum_{i=1}^{n} T_i \tag{19}$$

where N is the rotational speed at which the impeller was rotating, measured in radians per second [rad s^{-1}] and $\sum_{i=1}^{n} T_i$ is the sum of the moments exerted on the impeller surfaces and the shaft, measured in Newton-meters [N_m] that was obtained according to the CFD simulation results. The plot of N_P vs Reynolds number *(Re)* is presented in Fig. 6, where the mixing Reynolds number in stirred tanks was defined as $R_e = (\rho_l D^2 N)/\mu_l$.

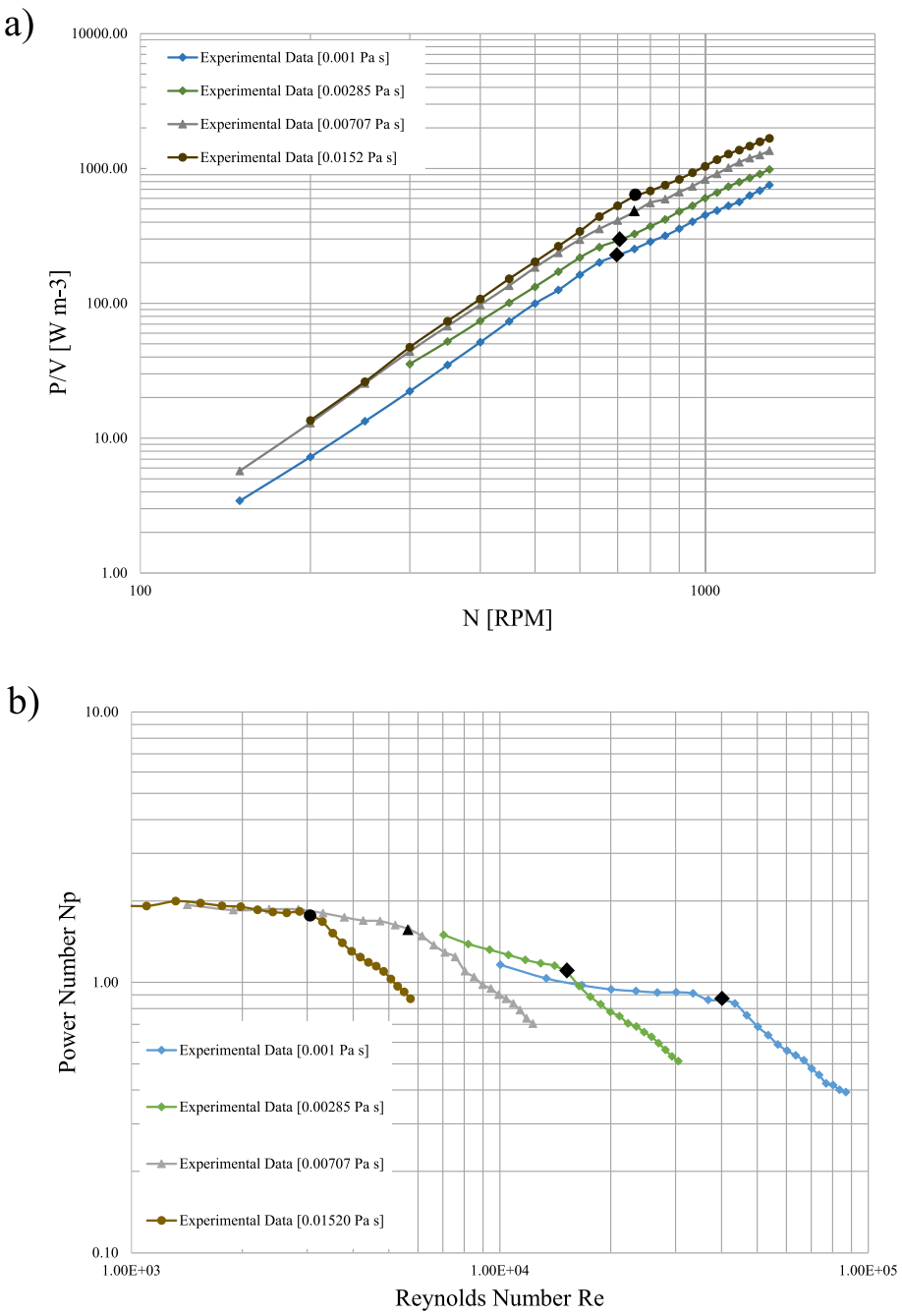

Fig. 5. Experimental specific power dissipation (a) and the respective power number (b) for liquid viscosities investigated (Scargiali et al., 2013).

The data for the power number *(Np)* were meticulously gathered for each specified liquid viscosity (0.001_Pa·s, 0.00285_Pa·s, 0.000707_Pa·s, and 0.00152_Pa·s) while maintaining constant impeller speeds at 200, 400, 600, 800, 1000, and 1200 RPM. This methodology enabled a comprehensive examination of different flow regimes:

- Sub-critical regime: in this regime, the vortex generated by the impeller did not yet reach the impeller itself. This phase was crucial for understanding the initial flow characteristics and the onset of vortex formation. The power number *(Np)* follows a well-defined law that was solely a function of the Reynolds number *(Re)*. During this phase, fluid behavior is primarily governed by the Reynolds number, representing the predominance of viscous terms over inertial ones.
- Supercritical regime: In the second regime, the vortex has fully reached the impeller, and the gas phase above the liquid is now being dispersed into the liquid as bubbles. This dispersion was significant as it affected the overall mixing efficiency and the homogeneity of the mixture. The behavior of the power number is influenced by a combination of two parameters: the Reynolds number *(Re)* and the Froude number *(Fr)* evaluated by the following expression $Fr = DN^2/g$, as reported in literature (Scargiali et al., 2013). The transition between these two regions is easily identifiable as it occurred when the Reynolds value reached a certain critical point, related to a specific critical velocity of the impeller (N_{crit}). This transition was associated with the onset of bubble ingestion and the reaching of the vortex at the impeller. In this phase, fluid behavior was influenced by both viscosity and inertial forces, and the Froude number began to play a significant role.

The distinction between these two regions is of fundamental

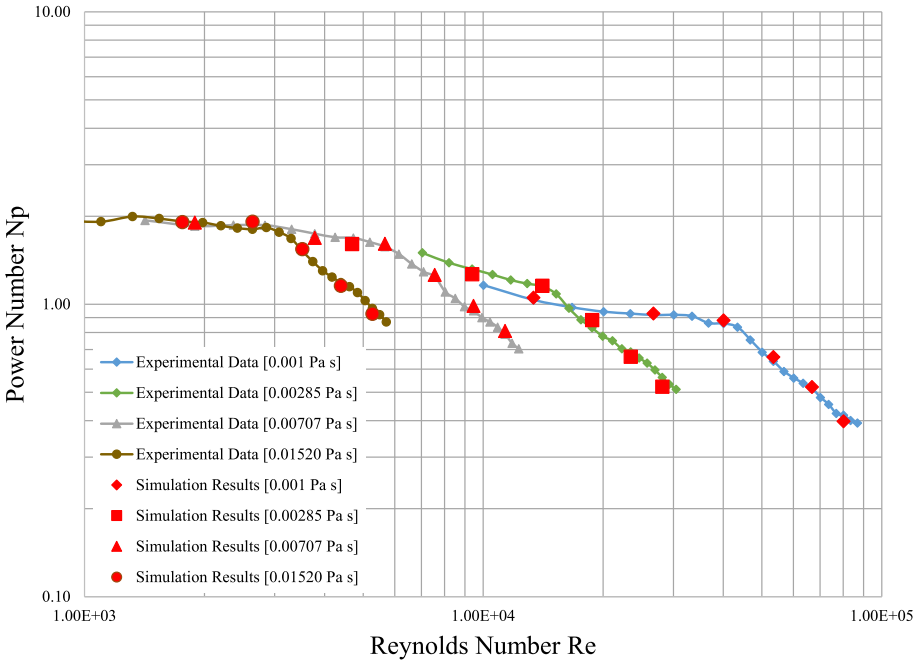

Fig. 6. Comparison between experimental data (Scargiali et al, 2013) and simulation results on Power number versus Reynolds number for various liquid viscosities.

importance as it indicated when significant changes in fluid behavior can be expected based on operational parameters. This transition was typically highlighted when the Reynolds value crossed a critical threshold, emphasizing the shift from a viscosity-dominated regime to one in which inertial forces and impeller speed significantly influence fluid behavior. As it can be seen, the results of numerical simulations shown in Fig. 6 exhibited excellent agreement with experimental data previously documented in the literature. This alignment underscored the robustness and accuracy of the computational fluid dynamics (CFD) modelling employed in this study. By capturing the complex flow dynamics and mixing behavior, the simulations validated the reliability of the chosen turbulence models and grid resolutions. This convergence between simulation and experimental results not only enhances confidence in the computational approach but was further corroborated by the noticeable change in slope observed in the N_{crit} value upon the vortex reaching the Rushton impeller. This underscores the utility of CFD as a predictive tool for optimizing design parameters and operational conditions in industrial applications, ensuring effective and efficient performance of fluid systems.

3.3. *Vortex shape simulation results*

Fig. 7 shows the impact of impeller speed on the shape of the free surface within a cylindrical agitated vessel for the liquid viscosity equal to 0.001_Pa·s. The simulations confirmed two distinct regimes based on impeller rotational speed. In the subcritical regime, at lower speeds, the vortex generated inside the vessel did not reach the impeller. The free surface remained relatively stable with minimal deformation. This regime signified more controlled and less turbulent conditions, (impeller velocity of 400 and 600 RPM). At higher speeds, the vortex reached the impeller, causing bubble self-ingestion and deformation of the free surface. This super-critical regime was associated with highly dynamic and turbulent fluid behavior. The analysis effectively visualized the transition between these regimes based on impeller speed. Understanding this relationship was crucial for optimizing fluid behavior within agitated vessels for various industrial processes.

The distinction between subcritical and supercritical regimes significantly impacted process efficiency and performance, influencing decisions about agitation speed, mixing strategies, and equipment design. In Fig. 7.*b* velocity profiles are also shown within the Uncovered Unbaffled Stirred Tank, confirming findings from the literature of the existence of two toroidal recirculations below and above the impeller, responsible for the vortex formation near the shaft (Xiong et al., 2023).

In this study, the free surface shape was analyzed through computational fluid dynamics simulations and compared with the correlations provided by Nagata, re-elaborated by Ciofalo et al. (Ciofalo et al., 1996) and the Two-Zone Model (2ZM) reported by Busciglio et al. (Busciglio et al., 2013). For the subcritical regime ($N = 600RPM$), the simulations, 2ZM and Nagata models were used to evaluate the free surface profile. Similarly, in the supercritical regime ($N = 800RPM$), the 2ZM and simulation solutions were utilized to determine the vortex shape. The Nagata model employed empirical correlations based on extensive experimental data to predict the free surface shape. Additionally, the two-zone model divided the tank into two distinct regions: an inner region dominated by rotational flow and an outer region where the flow is more radial.

These models were evaluated in comparison to the CFD simulations, which provide a more detailed and dynamic analysis of the fluid behavior within the tank. Notably, Nagata's predictions were provided solely for sub-critical impeller speeds, as this model was developed specifically for those conditions. The results indicated a high degree of overlap between the solutions under identical conditions, confirming the reliability and accuracy of both models in predicting the free surface profile. Fig. 8 shows the profiles of the free surface evaluated using the models: 2ZM, Nagata and the simulation solution obtained from the implementation of the Volume of Fluid model applying a compressive scheme.

In the subcritical regime (Fig. 8.*a),* the agreement among the Nagata model, 2ZM, and simulation results was excellent, demonstrating the robustness of these models in predicting the fluid surface under these conditions. For the supercritical regime *(*Fig. 8.*b),* the 2ZM and simulation results also showed a strong correlation, accurately capturing the complex central vortex formation that occurs at higher agitation speeds. This comprehensive analysis reinforces the validity of using CFD simulations to predict fluid dynamics in UUSTs.

The formation of these air cavities was associated with the ingestion of air into the flow (Fig. 9), affecting the overall fluid dynamics significantly (Maluta et al., 2021). They played a pivotal role in the mixing

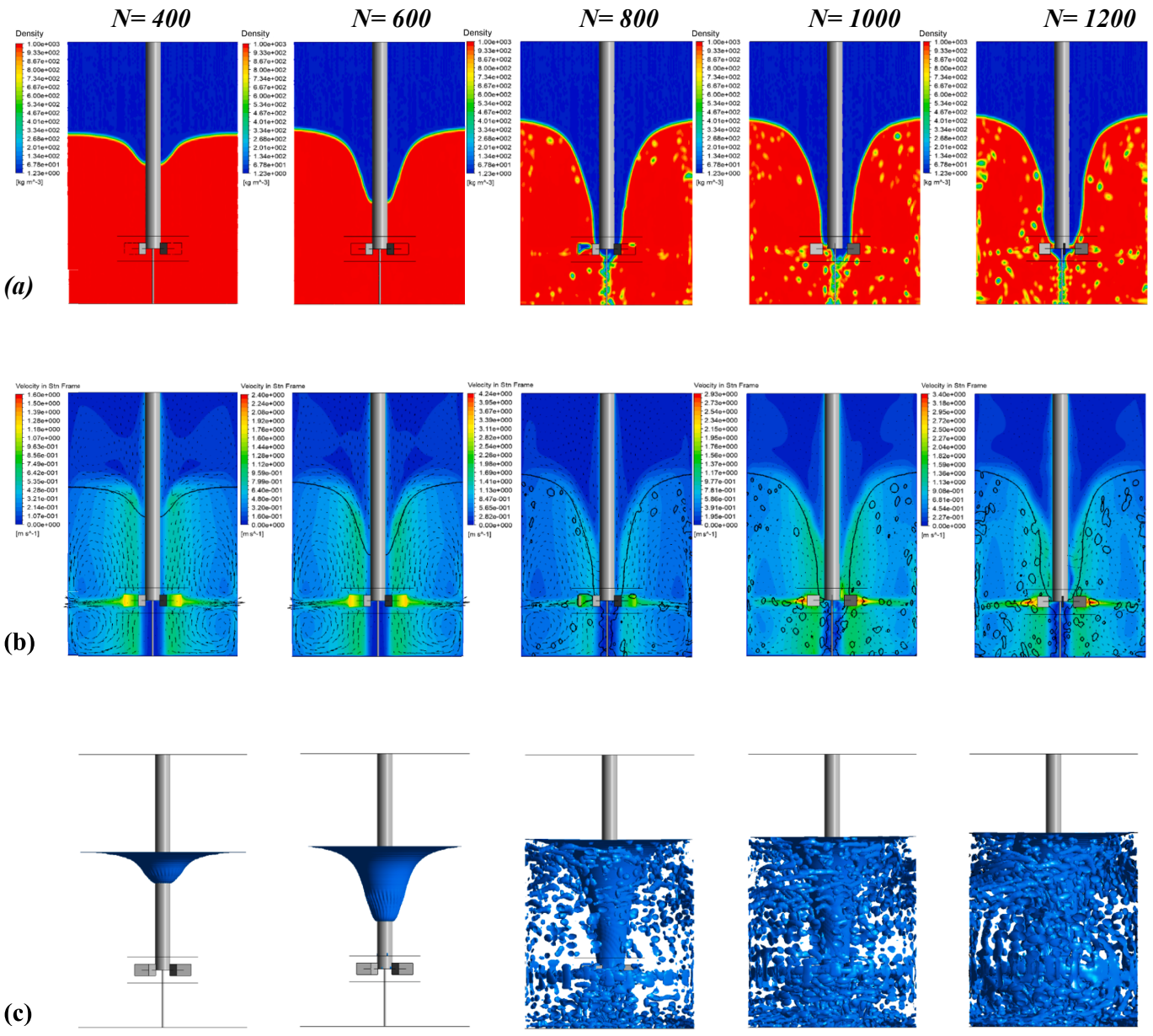

Fig. 7. Simulation results for a liquid viscosity of 0.001 Pa·s at various impeller speeds in RPM. (a) Vortex shape; (b) Velocity contours in a midplane with vector plot. Bold lines represent the free surface for a volume fraction of air equal to 0.1; (c) Isosurface of a volume fraction of air equal to 0.1.

process and mass transfer efficiency within the system. In the super-critical regime, the entrainment of air into the flow behind the impeller blades not only altered the flow patterns but also reduced the effective power consumption. This phenomenon underscored the complex interplay between fluid dynamics and operational parameters in stirred tanks, highlighting the importance of understanding and controlling such phenomena for optimizing mixing efficiency and process performance.

4. Conclusions

In this work, Computational Fluid Dynamics (CFD) simulations were employed to investigate the transition between non-aerated and aerated conditions in Uncovered Unbaffled Stirred Tanks (UUSTs). The Volume of Fluid (VOF) method effectively captured the free surface dynamics and vortex shapes under various impeller speeds. Different turbulence models were compared, and the Reynolds Stress Model with Linear Pressure-Strain Model (RSM-LPSM) was selected for its better internal consistency and its ability to predict both the shape and depth of the central vortex, as well as the values of the power number.

The Power Number (Np), evaluated using Ansys Fluent® fluid dynamics simulations, was plotted against the Reynolds Number (Re) for different liquid viscosities (0.001 Pa·s, 0.00285 Pa·s, 0.000707 Pa·s, 0.00152 Pa·s) at various impeller speeds (200, 400, 600, 800, 1000, 1200 RPM). The simulation results were able to predict the existence of two distinct regimes: sub-critical and super-critical. In the sub-critical regime ($N < N_{crit}$), the impeller speed was insufficient for the vortex to reach the blades, preventing air bubble entrainment. Conversely, the super-critical regime ($N > N_{crit}$) was characterized by vortex-induced bubble ingestion, leading to significant changes in power consumption and flow patterns. In the super-critical regime, air ingestion significantly altered the flow patterns reducing effective power consumption. This result emphasizes the role of air cavities in influencing power consumption and mixing efficiency within the stirred tank.

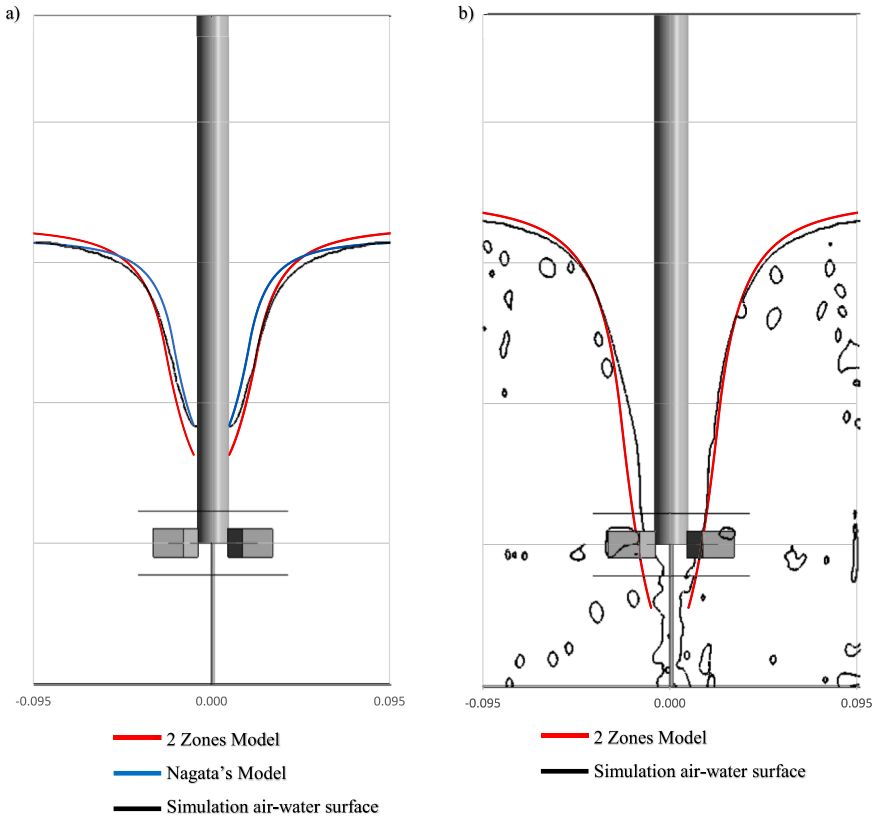

Fig. 8. Profiles of the free surface evaluated using the models: 2ZM (in red), Nagata (in blue) and the isosurface of a volume fraction of air equal to 0.1 (in black) for a) sub-critical regime (600 RPM) and b) super-critical regime (800 RPM).

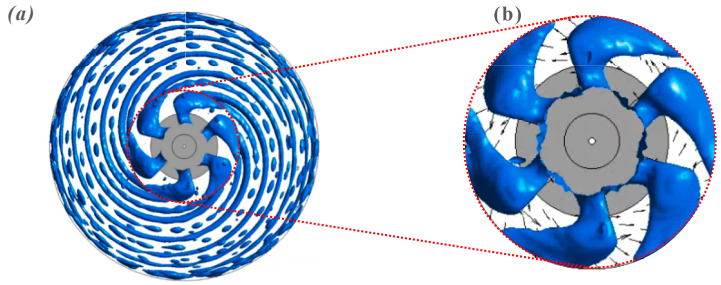

Fig. 9. Cavities behind the blades of a Rushton turbine in a supercritical stirred vessel (N = 800 RPM): (a) Isosurface of Volume Fraction of air equal to 0.1 on the plane of the impeller; (b) detail of cavities.

The transition from the sub-critical to the super-critical regime was well illustrated. In fact, it was marked by a noticeable change in the slope of the power number vs Reynolds number as the vortex reached the impeller, validating the simulation results against the experimental data.

Additionally, CFD simulations of the free surface shape at impeller speeds of 600 RPM (sub-critical) and 800 RPM (super-critical) were compared with two predictive models (Nagata model and Two-Zone Model, 2ZM). Simulation results showed excellent agreement with both models, confirming the accuracy of the CFD simulations in predicting free surface profiles. These findings underline the importance of CFD simulations for optimizing UUST design and operation, particularly when gas–liquid mass transfer is a key process consideration.

CRediT authorship contribution statement

Luca Schembri: Writing – original draft, Visualization, Validation, Software, Investigation, Formal analysis, Data curation. **Giuseppe Caputo:** Writing – review & editing, Supervision. **Michele Ciofalo:** Writing – review & editing, Visualization, Supervision, Methodology, Formal analysis, Data curation. **Franco Grisafi:** Supervision. **Serena Lima:** Writing – review & editing, Visualization, Supervision. **Francesca Scargiali:** Writing – review & editing, Visualization, Supervision, Methodology, Formal analysis, Conceptualization.

Declaration of competing interest

The authors declare that they have no known competing financial interests or personal relationships that could have appeared to influence the work reported in this paper.

Data availability

Data will be made available on request.

References

Alcamo, R., Micale, G., Grisafi, F., Brucato, A., Ciofalo, M., 2005. Large-eddy simulation of turbulent flow in an unbaffled stirred tank driven by a Rushton turbine. Chem. Eng. Sci. 60, 2303–2316. https://doi.org/10.1016/j.ces.2004.11.017.

Aloi, L.E., Cherry, R.S., 1996. Cellular response to agitation characterized by energy dissipation at the impeller tip. Chem. Eng. Sci. 51, 1523–1529. https://doi.org/10.1016/0009-2509(95)00307-X.

ANSYS Inc., 2021. Ansys Fluent Theory Guide. Release 2021 R2 ANSYS, Inc. 1069.

Bertrand, M., Parmentier, D., Lebaigue, O., Plasari, E., Ducros, F., 2012a. Mixing study in an unbaffled stirred precipitator using les modelling. Int. J. Chem. Eng. 2012. https://doi.org/10.1155/2012/450491.

Bertrand, M., Plasari, E., Lebaigue, O., Baron, P., Lamarque, N., Ducros, F., 2012b. Hybrid LES-multizonal modelling of the uranium oxalate precipitation. Chem. Eng. Sci. 77, 95–104. https://doi.org/10.1016/j.ces.2012.03.019.

Busciglio, A., Caputo, G., Scargiali, F., 2013. Free-surface shape in unbaffled stirred vessels: Experimental study via digital image analysis. Chem. Eng. Sci. 104, 868–880. https://doi.org/10.1016/j.ces.2013.10.019.

Busciglio, A., Grisafi, F., Scargiali, F., Brucato, A., 2014. Mixing dynamics in uncovered unbaffled stirred tanks. Chem. Eng. J. 254, 210–219. https://doi.org/10.1016/j.cej.2014.05.084.

Busciglio, A., Scargiali, F., Grisafi, F., Brucato, A., 2016. Oscillation dynamics of free vortex surface in uncovered unbaffled stirred vessels. Chem. Eng. J. 285, 477–486. https://doi.org/10.1016/j.cej.2015.10.015.

Ciofalo, M., Brucato, A., Grisafi, F., Torraca, N., 1996. Turbulent flow in closed and free-surface unbaffled tanks stirred by radial impellers. Chem. Eng. Sci. 51, 3557–3573. https://doi.org/10.1016/0009-2509(96)00004-8.

Daly, B.J., Harlow, F.H., 1970. Transport equations in turbulence. Phys. Fluids 13, 2634–2649. https://doi.org/10.1063/1.1692845.

Derksen, J., Van Den Akker, H.E.A., 1999. Large eddy simulations on the flow driven by a Rushton turbine. AIChE J. 45, 209–221. https://doi.org/10.1002/aic.690450202.

Deshpande, S.S., Kar, K.K., Walker, J., Pressler, J., Su, W., 2017. An experimental and computational investigation of vortex formation in an unbaffled stirred tank. Chem. Eng. Sci. 168, 495–506. https://doi.org/10.1016/j.ces.2017.04.002.

Escudié, R., Liné, A., 2006. Analysis of turbulence anisotropy in a mixing tank. Chem. Eng. Sci. 61, 2771–2779. https://doi.org/10.1016/j.ces.2005.09.022.

Fu, S., Huang, P.G., Launder, B.E., Leschziner, M.A., 1988. A comparison of algebraic and differential second-moment closures for axisymmetric turbulent shear flows with and without swirl. J. Fluids Eng. 110, 216–221. https://doi.org/10.1115/1.3243537.

Gibson, M.M., Launder, B.E., 1978. Ground effects on pressure fluctuations in the atmospheric boundary layer. J. Fluid Mech. 86, 491–511. https://doi.org/10.1017/S0022112078001251.

Glover, G.M.C., Fitzpatrick, J.J., 2007. Modelling vortex formation in an unbaffled stirred tank reactors. Chem. Eng. J. 127, 11–22. https://doi.org/10.1016/j.cej.2006.09.019.

Haque, J.N., Mahmud, T., Roberts, K.J., Rhodes, D., 2006. Modeling turbulent flows with free-surface in unbaffled agitated vessels. Ind. Eng. Chem. Res. 45, 2881–2891. https://doi.org/10.1021/ie051021a.

Jiao, Y., Zhang, Z., Gao, F., Han, J., Wang, J., 2024. Effects of particle suspension on surface vortex in unbaffled stirred tanks through DEM-VOF. Ind. Eng. Chem. Res. 63, 4662–4677. https://doi.org/10.1021/acs.iecr.3c04462.

Lamarque, N., Zoppé, B., Lebaigue, O., Dolias, Y., Bertrand, M., Ducros, F., 2010. Large-eddy simulation of the turbulent free-surface flow in an unbaffled stirred tank reactor. Chem. Eng. Sci. 65, 4307–4322. https://doi.org/10.1016/j.ces.2010.03.014.

Lamberto, D.J., Muzzio, F.J., Swanson, P.D., Tonkovich, A.L., 1996. Using time-dependent RPM to enhance mixing in stirred vessels. Chem. Eng. Sci. 51, 733–741. https://doi.org/10.1016/0009-2509(95)00203-0.

Launder, B.E., 1989. Second-moment closure and its use in modelling turbulent industrial flows. Int. J. Numer. Methods Fluids 9, 963–985. https://doi.org/10.1002/fld.1650090806.

Launder, B.E., Reece, G.J., Rodi, W., 1975. Progress in the development of a Reynolds-stress turbulence closure. J. Fluid Mech. 68, 537–566. https://doi.org/10.1017/S0022112075001814.

Launder, B.E., Spalding, D.B., 1974. The numerical computation of turbulent flows. Comput. Methods Appl. Mech. Eng. 3, 269–289. https://doi.org/10.1016/0045-7825(74)90029-2.

Li, L., Wang, J., Feng, L., Gu, X., 2017. Computational fluid dynamics simulation of hydrodynamics in an uncovered unbaffled tank agitated by pitched blade turbines. Korean J. Chem. Eng. 34, 2811–2822. https://doi.org/10.1007/s11814-017-0208-9.

Li, L., Xu, B., 2017. Numerical simulation of hydrodynamics in an uncovered unbaffled stirred tank. Chem. Pap. 71, 1863–1875. https://doi.org/10.1007/s11696-017-0180-1.

Lien, F.S., Leschziner, M.A., 1994. Assessment of turbulence-transport models including non-linear rng eddy-viscosity formulation and second-moment closure for flow over a backward-facing step. Comput. Fluids 23, 983–1004. https://doi.org/10.1016/0045-7930(94)90001-9.

Lima, S., Villanova, V., Grisafi, F., Brucato, A., Scargiali, F., 2020. Combined effect of nutrient and flashing light frequency for a biochemical composition shift in Nannochloropsis gaditana grown in a quasi-isoactinic reactor. Can. J. Chem. Eng. 98, 1944–1954. https://doi.org/10.1002/cjce.23776.

Lima, S., Brucato, A., Caputo, G., Schembri, L., Scargiali, F., 2022. Modelling nannochloropsis gaditana growth in reactors with different geometries, determination of kinetic parameters and biochemical analysis in response to light intensity. Appl. Sci. 12. https://doi.org/10.3390/app12125776.

Lima, S., Cosenza, A., Caputo, G., Grisafi, F., Scargiali, F., 2024. Utilization of native Chlorella strain in laboratory-scale raceway reactor for synthetic wastewater treatment: A study in batch and continuous modes with multi-substrate modeling. J. Water Process Eng. 60, 105145. https://doi.org/10.1016/j.jwpe.2024.105145.

Mahmud, T., Haque, J.N., Roberts, K.J., Rhodes, D., Wilkinson, D., 2009. Measurements and modelling of free-surface turbulent flows induced by a magnetic stirrer in an unbaffled stirred tank reactor. Chem. Eng. Sci. 64, 4197–4209. https://doi.org/10.1016/j.ces.2009.06.059.

Maluta, F., Paglianti, A., Montante, G., 2021. Prediction of gas cavities size and structure and their effect on the power consumption in a gas-liquid stirred tank by means of a two-fluid RANS model. Chem. Eng. Sci. 241, 116677. https://doi.org/10.1016/j.ces.2021.116677.

Maluta, F., Alberini, F., Paglianti, A., Montante, G., 2023. Hydrodynamics, power consumption and bubble size distribution in gas-liquid stirred tanks. Chem. Eng. Res. Des. 194, 582–596. https://doi.org/10.1016/j.cherd.2023.05.006.

Menter, F.R., Kuntz, M., Langtry, R., 2003. Ten years of industrial experience with the SST Turbulence Model Turbulence heat and mass transfer. Cfd. Spbstu.ru 4, 625–632.

Michalcová, V., Kotrasová, K., 2020. The numerical diffusion effect on the cfd simulation accuracy of velocity and temperature field for the application of sustainable architecture methodology. Sustain. 12, 1–18. https://doi.org/10.3390/su122310173.

Montante, G., Bakker, A., Paglianti, A., Magelli, F., 2006. Effect of the shaft eccentricity on the hydrodynamics of unbaffled stirred tanks. Chem. Eng. Sci. 61, 2807–2814. https://doi.org/10.1016/j.ces.2005.09.021.

Moucha, T., Linek, V., Prokopová, E., 2003. Gas hold-up, mixing time and gas-liquid volumetric mass transfer coefficient of various multiple-impeller configurations: Rushton turbine, pitched blade and techmix impeller and their combinations. Chem. Eng. Sci. 58, 1839–1846. https://doi.org/10.1016/S0009-2509(02)00682-6.

Nagata, S., 1975. Mixing – Principles and Applications. Halsted Press, Tokyo, Japan.

Ngo, T.A., Nguyen, T.H., Bui, H.T.V., 2012. Thermophilic fermentative hydrogen production from xylose by Thermotoga neapolitana DSM 4359. Renew. Energy 37, 174–179. https://doi.org/10.1016/j.renene.2011.06.015.

Nienow, A.W., Warmoeskerken, M.M.C.G., Smith, J.M., Konno, M., 1985. On the flooding/ loading transition and the complete dispersal condition in aerated vessels agitated by a Rushton turbine. 5th Eur. Conf. Mix. Wurzburg, West Ger. 143–154. https://doi.org/10.1016/0009-2509(87)85067-4.

Płusa, T., Talaga, J., Duda, A., Duda, P., 2021. Modeling mixing dynamics in uncovered baffled and unbaffled stirred tanks. AIChE J. 67, 1–17. https://doi.org/10.1002/aic.17322.

Prakash, B., Bhatelia, T., Wadnerkar, D., Shah, M.T., Pareek, V.K., Utikar, R.P., 2019. Vortex shape and gas-liquid hydrodynamics in unbaffled stirred tank. Can. J. Chem. Eng. 97, 1913–1920. https://doi.org/10.1002/cjce.23433.

Ramírez-Cruz, J., Salinas-Vázquez, M., Ascanio, G., Vicente-Rodríguez, W., Lagarza-Córtes, C., 2020. Mixing dynamics in an uncovered unbaffled stirred tank using Large-Eddy Simulations and a passive scalar transport equation. Chem. Eng. Sci. 222, 115658. https://doi.org/10.1016/j.ces.2020.115658.

Rushton, J.H., Costich, E.W., Everett, H.J., 1950. Power characteristics of mixing impellers – part II. Chem. Eng. Prog. 46, 467–476. https://doi.org/10.1016/b978-012220855-3/50007-9.

Scargiali, F., Busciglio, A., Grisafi, F., Tamburini, A., Micale, G., Brucato, A., 2013. Power consumption in uncovered unbaffled stirred tanks: influence of the viscosity and flow regime. Ind. Eng. Chem. Res. 52, 14998–15005. https://doi.org/10.1021/ie402466w.

Scargiali, F., Busciglio, A., Grisafi, F., Brucato, A., 2014. Mass transfer and hydrodynamic characteristics of unbaffled stirred bio-reactors: Influence of impeller design. Biochem. Eng. J. 82, 41–47. https://doi.org/10.1016/j.bej.2013.11.009.

Scargiali, F., Tamburini, A., Caputo, G., Micale, G., 2017. On the assessment of power consumption and critical impeller speed in vortexing unbaffled stirred tanks. Chem. Eng. Res. Des. 123, 99–110. https://doi.org/10.1016/j.cherd.2017.04.035.

Speziale, C.G., Sarkar, S., Gatski, T.B., 1991. Modelling the pressure–strain correlation of turbulence: an invariant dynamical systems approach. J. Fluid Mech. 227, 245–272. https://doi.org/10.1017/S0022112091000101.

Tamburini, A., Cipollina, A., Micale, G., Scargiali, F., Brucato, A., 2016. Particle suspension in vortexing unbaffled stirred tanks. Ind. Eng. Chem. Res. 55, 7535–7547. https://doi.org/10.1021/acs.iecr.6b00824.

Tamburini, A., Brucato, A., Ciofalo, M., Gagliano, G., Micale, G., Scargiali, F., 2021. CFD simulations of early- to fully-turbulent conditions in unbaffled and baffled vessels stirred by a Rushton turbine. Chem. Eng. Res. Des. 171, 36–47. https://doi.org/10.1016/j.cherd.2021.04.021.

Tanaka, M., Noda, S., O'shima, E., 1986. Effect of the location of a submerged impeller on the enfoldment of air bubbles from the free surface in a stirred vessel. Int. Chem. Eng. 26, 314–318.

Xiong, X., Wang, S., Liu, P., Tao, C., Wang, Y., Liu, Z., 2023. Numerical investigation on intensified mixing performance with modified dual impeller. Chem. Eng. Sci. 274. https://doi.org/10.1016/j.ces.2023.118698.

Zamiri, A., Chung, J.T., 2017. Ability of URANS approach in prediction of unsteady turbulent flows in an unbaffled stirred tank. Int. J. Mech. Sci. 133, 178–187. https://doi.org/10.1016/j.ijmecsci.2017.08.008.